Atmos. Chem. Phys. Discuss., 14, 31483–31514, 2014
www.atmos-chem-phys-discuss.net/14/31483/2014/
doi:10.5194/acpd-14-31483-2014

Atmospheric Chemistry and Physics Discussions

A comprehensive investigation on afternoon–evening transition of the atmospheric boundary layer over a tropical rural site

A. Sandeep[1], **T. Narayana Rao**[1], **and S. V. B. Rao**[2]

[1]National Atmospheric Research Laboratory, Gadanki – 517 112, India
[2]Sri Venkateswara University, Department of Physics, Tirupati – 517 502, India

Received: 30 October 2014 – Accepted: 11 November 2014 – Published: 12 December 2014

Correspondence to: T. Narayana Rao (tnrao@narl.gov.in)

Published by Copernicus Publications on behalf of the European Geosciences Union.

Abstract

The transitory nature of the atmospheric boundary layer few hours before and after the time of sunset has been studied comprehensively over a tropical station, Gadanki (13.45° N, 79.18° E), using a suite of in-situ and remote sensing devices. This study addresses the following fundamental and important issues related to the afternoon-to-evening transition (AET). Which state variable first identifies it? Which variable best identifies it? Does the start time of AET varies with season and height? If so, which physical mechanism is responsible for the observed height variation in the start time of transition?

The transition is seen first in temperature (T) and wind variance (σ^2_{ws}) variations at the surface, ∼ 100 min prior to the time of sunset, then in vertical temperature gradient and finally in water vapour mixing ratio variation. Aloft, the AET is observed nearly at the same time in signal to noise ratio (SNR) and spectral width (σ) measurements of wind profiler and sodar. The T at the surface and SNR aloft identify the signature of transition unambiguously. Also, their distributions for start time of AET with reference to the time of sunset are narrow and consistent in total and seasonal plots. The start time of transition shows some seasonal variation with delayed transitions occurring mostly in the rainy and humid season of northeast monsoon. Interestingly, in contrast to the general perception, the signature of the transition is first seen in the profiler data then in sodar data and finally in the surface data, suggesting that the transition follows top-to-bottom evolution. It indicates that other forcings, like entrainment, play a major role in altering the structure of ABL during the AET, when the sensible heat flux decreases progressively. These forcing terms are quantified using a unique high-resolution dataset to understand their variation in light of the intriguing height dependency of the start time of AET.

ACPD
14, 31483–31514, 2014

1 Introduction

The behaviour of atmospheric boundary layer (ABL) during the transition from well mixed layer during the day to stably stratified layer during the night is quite complex and is also poorly understood. In recent years, the afternoon to evening transition (AET) of the ABL gained lot of attention for various reasons (Lothon et al., 2014). These transitional regimes are found to be important for the vertical transport of species, like pollutants, water vapour and ozone (Klein et al., 2014), the inception and strength of the nocturnal low level jet (LLJ) (Mahrt, 1981; Van De Wiel et al., 2010), and the whole structure of the nocturnal boundary layer. Further, identification of ABL becomes uncertain and there is no consensus on which scaling laws (day-time convective scaling due to surface buoyancy flux? or nocturnal boundary layer scaling due to surface wind stress?) would work well during this period (Pino et al., 2006). Further, the start time of transition and its duration could be different at the surface and aloft, because the turbulence may not immediately dissipate after the sunset (Busse and Knupp, 2012).

Researchers defined the evening transition in a variety of ways employing various parameters obtained from different instruments. Some of them treated the transition as an instantaneous process, while the others considered it as a process of few hours. The most popular and widely used definition is the reversal of surface heat flux (positive to negative) (Grant, 1997; Acevedo and Fitzjarrald, 2001; Beare et al., 2006; Angevine, 2008). A similar technique is employed by Nieuwstadt and Brost (1986), in which the AET is assumed to occur following the cessation of upward surface sensible heat flux. Edwards et al. (2006) noted that the shortwave heating starts to decrease much before the surface heat flux changes its sign. They included the shortwave heating in the definition of AET, which shifted the start of evening transition to an earlier time. Acevedo and Fitzjarrald (2001) identified the start time of transition from a sharp decrease in the spatial temperature difference and end from the maximum spatial standard deviation (SD) of temperature. As seen above, all these definitions are based on surface

ACPD
14, 31483–31514, 2014

measurements and do not account the physical processes occurring aloft during the transition.

The studies that used remote sensing measurements like wind profiling radars, sodars and lidars focused more on the processes aloft (mostly in the lower part of ABL) to define the AET. In a seminal study, Mahrt (1981) used a kinematic definition for AET period. According to Mahrt (1981), the AET is a 4–5 h time period, starts from the time of low-level wind deceleration (typically 2 h before the sunset) and ends when the flow at all levels turned towards the high pressure. Grimsdell and Angevine (2002) and Angevine (2008), using radar wind profiler measurements, noticed that both reflectivity (range-corrected signal-to-noise-ratio (SNR)) and the spectral width (σ) (a measure of turbulence) decrease sharply during the AET. The applicability of these approaches is always an issue, particularly when the turbulence is either weak or strong throughout the day or when the turbulence increases due to some other processes associated with katabatic winds or land see-breeze circulations (Sastre et al., 2012). Instead of defining the start and end times for AET, Busse and Knupp (2012) studied the variations in meteorological parameters with reference to the sunset time. They noted an increase in wind speed and a decrease in sodar return power in the lower ABL. They found that the AET has a relatively consistent pattern regardless of season.

A few studies employed models to understand or validate the occurrence of different types of transition (Brazel et al., 2005; Edwards et al., 2006; Pino et al., 2006; Sorbjan, 2007; Nadeau et al., 2011; Sastre et al., 2012). Brazel et al. (2005) studied the evening transition under weak synoptic forcing that favours the local thermal circulations and compared the observed transitions with models. Recently, Sastre et al. (2012) identified 3 types of evening transitions and evaluated performance of the Weather Research and Forecasting Advanced Research (WRF-ARW) model in reproducing these transitions by varying PBL parameterization schemes. They noted that all parameterizations reproduced the observed behaviour of AET in certain circumstances. Noting the need to understand the evening transitions in a better way, several field campaigns were conducted in recent years, employing both in situ and remote sensors, exclusively for bet-

ACPD
14, 31483–31514, 2014

ter characterisation and modelling of the evening transitions. For instance, Cooperative Atmosphere–Surface Exchange Study (CASES-99) (Poulos et al., 2002), Boundary Layer Late Afternoon and Sunset Turbulence (BLLAST) (http://bllast.sedoo.fr/) (Lothon et al., 2014) and Phoenix Evening Transition Flow Experiment (TRANSFLEX) (Fernando et al., 2013). Recently, manned and unmanned aerial vehicles were used to study the vertical structure of lowest part of ABL during the AET (Bonin et al., 2013; Lothon et al., 2014).

Most of the above studies focussed on the variations in state variables, like temperature, humidity, wind and turbulence, in the surface layer as they are easily accessible. Other studies characterized the evening transitions aloft, but neglecting the variations at the surface. Only a few studies that were based on campaign data and/or a few months of data dealt the transitions in totality, i.e., studied the variations at the surface and aloft (Busse and Knupp, 2012; Fernando et al., 2013; Lothon et al., 2014). Again, the data employed in those studies were limited, few days to 2 months. Certainly there is a need to characterize and understand the transitions at the surface and aloft in different seasons through systematic observations on a long-term basis. Further, earlier studies used different state variables to define the transition. Only a few studies focused on how these state variables vary with reference to the time of sunset (Busse and Knupp, 2012). Although some tower-based observations exist in the literature, the complete understanding of the transition over a deeper layer is certainly far from complete. This forms the basis for the present study. In particular, the study tries to address the following questions: how the surface state variables and radar/sodar attributes vary during the transition and with reference to the time of sunset? Which state variable better identifies the transition? How the start time of transition varies with height and season? Which physical processes are responsible for the vertical evolution of the transition?

The paper is organized as follows: Sect. 2 introduces the measurement site, data and instrumentation employed. The variation of different state variables at the surface and aloft is studied with the help of a typical case study in Sect. 3. The start time

ACPD
14, 31483–31514, 2014

of AET as identified by different state variables and their mean characteristics at the surface and aloft are studied with reference to the start time of transition. The questions posed above are discussed in the light of present observations in Sect. 4. The important forcing terms on the ABL are estimated using a unique dataset to understand the role of entrainment in the evening transitions. The important results are concluded in Sect. 5.

2 Data and site description

The present study follows an integrated approach, wherein several instruments available at National Atmospheric Research Laboratory (NARL), Gadanki (13.45° N, 79.18° E) are extensively used. This site is located ~ 375 m above the mean sea level in a rural area in southeast peninsular India and is surrounded by hillocks (300–800 m within 10 km region) distributed in a complex fashion. The rainfall in this region is influenced primarily by two monsoons, southwest (June–September) and northeast (October–December) (Rao et al., 2009). Summer and winter are the other two seasons, covering the months of March–May and January–February, respectively.

The present study relies on a variety of instruments, both in situ and remote sensors (Table 1), whose measurements cover the entire ABL. Though these instruments provide several other parameters, those used in the present study are only listed in Table 1. Two kinds of datasets are used in the present study, but for different purposes. To study the vertical structure and the seasonality in AET, long-term observations made by an instrumented 15 m tower (hereafter referred to as Mini Boundary Layer Mast – MBLM), a Doppler sodar and three UHF wind profilers (operated at NARL, but during different years) have been used. Whereas, few days of intense observations made by a flux tower and GPS radiosonde (one ascent in 3 h) have been used to understand the role of surface forcing and entrainment in triggering the AET.

The MBLM provides temperature (T), relative humidity (RH), wind speed (WS) and wind direction (WD) data at 3 levels (5, 10 and 15 m) with 1 s temporal resolution. The type of sensors used and their accuracies are given in Table 2. A Doppler sodar operat-

ACPD
14, 31483–31514, 2014

ing at a frequency of 1.8 kHz and a peak power of 100 W provides the SNR, σ and wind information at 27 s and 30 m temporal and height resolutions, respectively (Anandan et al., 2008) (see Table 3 for more details about different remote sensing instruments). The UHF wind profiler data consists of the data from 3 wind profilers, operated during different years. An old UHF wind profiler (referred to as Lower Atmospheric Wind Profiler – LAWP) was operated at a frequency of 1.375 GHz during the period 1999–2000. Complete description of the system and specifications can be found in Reddy et al. (2001) and Rao et al. (2001). It was operated in two modes; low mode covering 0.3 to 4.8 km and high mode covering 0.9 to 6.8 km, sequentially switching between each mode, providing a temporal resolution of $\sim$ 11 min. Recently, NARL has indigenously developed two UHF wind profilers with the same frequency (1.28 GHz) but with different antenna dimensions and transmitted powers. The smaller UHF wind profiler that uses an 8×8 antenna array covering an area of 1.4 m $\times$ 1.4 m transmits a power of 0.8 kW (hereafter referred to as $\mathrm{WPR}_{8\times8}$). Whereas, the larger profiler has a bigger antenna array of 2.8 m $\times$ 2.8 m with 16×16 elements and high-transmitting power of 1.2 kW (hereafter referred to as $\mathrm{WPR}_{16\times16}$). Complete description of these systems and their capabilities can be found in Srinivasulu et al. (2011, 2012). The $\mathrm{WPR}_{8\times8}$ was operated at NARL during May–September 2010, while the bigger $\mathrm{WPR}_{16\times16}$ has been in operation from October 2010. It can be seen from Tables 1 and 3 that these instruments provide a unique long-term dataset from the surface to top of the ABL.

These long-term measurements are augmented by intense observations made in a campaign, wherein GPS radiosondes (Meisei 90) have been launched for every 3 h for 3 successive days. Also a 50 m micrometeorological flux tower housing a sonic anemometer (RM Young 8100) at 8 m level (with 20 Hz temporal resolution) is also employed for the estimation of sensible heat flux. Two such campaigns were conducted, one each in monsoon and winter.

A series of automated tests were performed on tower time series data to identify instrumentation problems, flux sampling problems, and physically plausible but unusual situations. Further, clear-sky days are identified from shortwave radiation measure-

ACPD
14, 31483–31514, 2014

ments made by a pyranometer (Kipp and Zonen CMP6) located near the MBLM. Omitting the days with large data gaps and rain/dense clouds, 423 days of surface data were available for further analysis from 3 years of MBLM measurements. The range-time plots of spectral moments (SNR, vertical velocity (w) and σ) from sodar and wind profiler are examined for the clear growth and decay of ABL and convection/precipitation contamination (Grimsdell et al., 2002; Rao et al., 2008). Based on the above criteria, a total of 530 and 482 clear-sky days of sodar and radar, respectively, were only selected for further analysis. Note that MBLM, sodar and wind profilers were operated during different years. Only 19 days of simultaneous clear-sky measurements (without large data gaps) from all the above sensors were available. Measurements from these 19 days are used to understand the behavior of AET at different altitudes. The total data (from different years) are used to obtain robust statistics on the mean behavior of AET.

3 Results and discussion

3.1 Typical evolution of AET from the surface to top of the ABL

Figure 1 shows the diurnal variation of surface state variables (T, water vapour mixing ratio (r), WS and wind variance (σ^2_{ws})) and sodar and profiler attributes (SNR, horizontal wind speed, σ and w) on 11 May 2010, providing a comprehensive paradigm of the typical evolution of evening transitional boundary layer at the surface and aloft (up to 3.6 km). The surface state variables (at 5 m level) exhibit larger variations during the transition period than during rest of the night. During the AET, as the shortwave heating decreases, the temperature decreases monotonically (Fig. 1a) in clear-sky conditions, if temperature advection is neutral. Another signature of this transition can be seen in short-term variability of surface parameters, highly variable during the noon (associated with thermals) to smaller fluctuations in the night. The weakening of thermals (both magnitude and their vertical extent) in the afternoon reduces the convective tur-

ACPD
14, 31483–31514, 2014

bulence and σ^2_{ws} (Fig. 1d). This reduction weakens the downward transport of momentum and low-level wind speed (Fig. 1c) (Mahrt, 1981; Acevedo and Fitzjarrald, 2001). The surface winds also became less gusty during the transition. During the day, when the convective turbulence is active, the low-level moisture gets diluted because of the transport of moisture by turbulence. As the turbulence decreases during the transition, the low-level moisture having most of its sources on the earth's surface increases in the absence of strong mixing (Fig. 1b). On some days, this increase appears as a sudden jump, as also noted by earlier studies (Busse and Knupp, 2012), and on the other days it is more gradual.

To understand the transitions aloft, variation of sodar and profiler attributes are examined in detail (Fig. 1e–l). Figure 1 clearly shows the transition of the ABL from a highly convective to a more stable regime. When the convective turbulence is active during the day time, the thermals are clearly apparent as columns of enhanced backscatter in the time-height SNR plot (Fig. 1e and i). These plumes are also visible in the w plot (Fig. 1h and l) as enhanced up- and down-ward motions with w values exceeding $\pm 2\,\mathrm{m\,s^{-1}}$ and as columns of enhanced turbulence (Fig. 1f and j). The backscatter for sodar and radar depends on the refractive index irregularities caused primarily by turbulence-driven temperature and humidity variations. The SNR is, therefore, high during the day, when the convectively-driven turbulence is active. Nevertheless, about 2 h before the sunset, both the intensity and vertical extent of thermals start to decrease with time before they became horizontally stratified. The minimum backscatter (SNR) is seen just before the sunset, mainly due to the weak turbulence. The magnitude of backscatter and vertical extent of sodar data again increase in accordance with the deepening of the inversion layer. As noted by Busse and Knupp (2012), the winds within the nocturnal boundary layer generally decrease during the AET, but increase above the nocturnal boundary layer. It makes the identification of start time of AET using wind speed somewhat ambiguous. On the other hand, it is rather easy to identify the start time of AET from the variations of SNR and σ.

ACPD
14, 31483–31514, 2014

When the surface heating reverses to cooling in the evening, both convection and turbulence gradually reduces till the subsequent development of a stable boundary layer with well-defined surface inversion layer. As a result, all state variables at the surface and aloft, manifested primarily by the turbulence, vary considerably during this period. To better depict this variability, MBLM- (T, r, σ^2_{ws} and ΔT ($T_5 - T_{10}$, indicating the stability of the lower ABL, the suffixes 5 and 10 indicate the height of temperature measurements in m)), sodar- and profiler-derived state variables (SNR and σ at 3 representative levels; 150, 300 and 450 m for sodar and 900, 1500 and 2100 m for radar) during the period 15:00–21:00 IST (Indian Standard Time (IST) = UTC + 05:30) are plotted in Fig. 2. To minimize random fluctuations and the chosen level more representative, the data are averaged both in time (5 min for sodar and no temporal integration for radar) and height (3 heights centred on the chosen level). On 11 May 2010, the temperature (Fig. 2a) starts to decrease monotonically, at the rate of 1–1.5 °C per 1 h, from 16:45 IST (dashed line), 118 min prior to the time of sunset (solid vertical black line). Though the temperature decrement starts little early, but is not consistent and also weak in magnitude. Another surface characteristic showing a significant change during the AET is the mixing ratio (Fig. 2b), which clearly shows a gradual increase from 16:10 IST. The temperature gradient (Fig. 2c) also reverses from positive to negative, indicating the reversal of surface sensible heat flux, few minutes after the 5 m level temperature starts to decrease. The wind variance (Fig. 2d), representing small-scale wind fluctuations and turbulence, also shows a decreasing trend from 16:45 IST.

The sodar and profiler backscatter, depends primarily on turbulent irregularities of refractive index, decreases with the waning of sensible heat flux (and thermals) during the afternoon transition. On 11 May 2010, the SNR of sodar starts to decrease ~ 2 h 40 min prior to the time of sunset at all heights. Interestingly, the start time of SNR reduction shows height dependence with higher altitudes showing the reduction earlier. The SNR minimum is observed 10–20 min before the sunset at all heights, mainly due to the reduction in turbulent fluctuations in temperature. Nevertheless, the SNR increases again after the sunset, following the formation of an inversion layer. The σ

ACPD
14, 31483–31514, 2014

(Fig. 2f) variations are quite similar to that of SNR during the transition. The σ shows a decreasing trend 2 h 10–20 min prior to the sunset, whereas its minimum is observed 10–30 min from the time of sunset. The profiler SNR and σ variations are similar to that of sodar, except that their reduction starts little early. The profiler SNR and σ start to decrease $\sim$ 3 h prior to the time of sunset. Also, the SNR and σ minima are observed at around the time of sunset. It is very interesting to note the height dependency in the time at which state variables show large variation, i.e., it is seen first in profiler attributes then in sodar attributes and finally in surface parameters.

3.2 Distributions for start time of transition with reference to the time of sunset

It is clear from the case study that surface parameters and sodar/profiler attributes show large variations during the AET. The first and foremost problem, therefore, is to properly and objectively identify the start time of AET from these state variables. It is also important to recognize the state variable that unambiguously identifies the start time of transition. As seen in case studies, state variables like T, ΔT, r and σ^2_{ws} at the surface and SNR and σ aloft can be used for this purpose. For identifying the start time of AET, 19 days on which measurements of all instruments (MBLM, sodar and profiler) are available are considered. The start time of AET is identified manually from the temporal variation of each state variable (like those shown in Fig. 2). The temporal gradients are estimated for each state variable from all 19 cases, which are then finally used to fix the thresholds. The start time of AET is identified from the variation of the each state variable as follows.

Temperature: the time at which T starts to decrease by $\geq 0.5\,^{\circ}$C in 30 min.

Water vapour mixing ratio: the time at which r increases by $\geq 0.5\,\mathrm{g\,kg^{-1}}$ in 30 min.

Wind variance: the time at which σ^2_{ws} decreases by $\geq 0.1\,\mathrm{m^2\,s^{-2}}$ in 30 min.

Temperature gradient: the time at which ΔT becomes positive to negative and remains negative for at least an hour.

ACPD
14, 31483–31514, 2014

SNR: the time at which SNR decreases by > 1 dB in 30 min.

Spectral width: the time at which σ decreases by $\geq 0.1\,\mathrm{m\,s^{-1}}$ in 30 min.

Note that all the above conditions should hold good for at least an hour from the start time of transition. Also, all the above conditions are checked only in the data during 15:00–20:00 IST.

First, the average behaviour of the start time of AET, as identified by selected state variables, with reference to the sunset (i.e., start time of AET – time of sunset) has been studied at the surface and aloft. The distributions (from the whole dataset) for start time of AET with reference to the sunset (hereafter referred to as $\mathrm{Trans_{sunset}}$ (start time of AET – time of sunset)) as obtained by various state variables are shown in Fig. 3. These distributions are shown as box plots, where the box comprises 50 % of values (25 and 75 percentile) and whiskers represent 5 and 95 % percentile values. On average, σ^2_{ws} and T show the first signature of AET among all surface state variables (Fig. 3a), ~ 1 h 40 min prior to the time of sunset, followed by ΔT (1 h 18 min before sunset). The last characteristic for transition is seen in r as a gradual increase (or jump) occurring, 1 h 10 min prior to the time of sunset. The signature of transition can be seen as early (late) as 165 (45) min before (after) the sunset in wind variance (r) on some days. Except for temperature, all other surface state variables show signature of transition even after the sunset. Though not many such cases are found at Gadanki (can be seen from Fig. 3a), but late evening transitions are not uncommon, as they are widely reported elsewhere (Acevedo and Fitzjarrald, 2001). The distribution of $\mathrm{Trans_{sunset}}$ is wider for r than for any other state variable, indicating that the jump in r occurs at different timings with reference to the time of sunset. On the other hand, the start time of AET as obtained by T is relatively consistent throughout the year, as evidenced by the narrow distribution (Fig. 3a).

Figure 3b–g shows distributions for $\mathrm{Trans_{sunset}}$ as identified by selected sodar and profiler attributes (SNR and σ) at 3 selected altitudes (150, 300 and 450 m for sodar and 900, 1500 and 2100 m for radar). On average, both SNR and σ show the signature of

ACPD
14, 31483–31514, 2014

transition around the same time. Though small differences exist, they are not significant and do not show any consistent pattern with altitude or between the radar and sodar. Nevertheless, the identification of transition start time is somewhat easy with SNR and is also consistent, as evidenced by its relatively narrow distribution.

As seen in the case study, the mean start time of AET also shows height dependency and follows top-to-bottom evolution, i.e, the signature of AET is seen first in the profiler data (~ 2 h 40 min before the time of sunset) then in sodar data (~ 2 h before the time of sunset) and finally in MBLM measurements. Angevine (2008) also noted the deterioration of ABL structure aloft with wind profiler preceding the start time of AET at the surface. It contradicts the general perception that the entire ABL is controlled primarily by the underlying earth's surface and the start time of transition should follow a bottom-up evolution. It is true that surface forcing is the defining mechanism during the day, but it seems not the case during the transition, the time during which other forces could also be important.

3.3 Seasonal variation in the start time of transition

Since Gadanki experiences different seasonal patterns: very hot and dry summer, hot and rainy southwest monsoon, cool and rainy northeast monsoon and cool and dry winter. These seasonal factors (solar exposure, synoptic flow, soil condition, etc.) will have a different impact on ABL, in general, transitions, in particular. Therefore, the distributions of $\text{Trans}_{\text{sunset}}$ for different seasons (Fig. 4) have been studied to understand the impact of the above factors on the start time of transition. Figure 4a–d reveals that the order in which the surface state variables show the transition remain nearly the same (monsoon season is an exception), but their occurrence time with reference to the sunset varies considerably. Although reduced compared to the total data (Fig. 3), the distribution, representing the variability within the season, of transition start time for each state variable is quite wide. The $\text{Trans}_{\text{sunset}}$ distribution for T shows a consistent pattern regardless of season with small variability within the season and the transition starts 80–100 min prior to the time of sunset. Nevertheless, it exhibits a clear

ACPD
14, 31483–31514, 2014

seasonal variation with dry seasons (winter and summer) showing the transition early (∼ 110 min prior to the sunset time) compared to rainy seasons (80 min prior to the sunset time). The distributions for other state variables also show some seasonal variation with warm seasons showing the transition little earlier than cold seasons. But their distributions are much wider than the observed weak seasonal variation. Among all state variables, $\text{Trans}_{\text{sunset}}$ distribution for r shows not only large seasonal variability but also a wide distribution, indicating highly variable nature of r jump (i.e., starts at different timings with reference to the sunset).

Two representative heights, 300 m from sodar and 1.5 km from wind profiler, are chosen to study the seasonal variation in transition start time aloft (Fig. 4e–l). Like in Fig. 3, there is not much difference in the start time of transition by SNR and σ. Two observations are strikingly apparent from Fig. 4. 1. Both profiler- and sodar-derived start time of transition shows some seasonal variation with delayed transition during the northeast monsoon, consistent with the seasonal variation at the surface. 2. Irrespective of the season, the height dependency in transition start time is intact. Both these issues are discussed in detail in Sect. 4.

4 Discussion

The three major questions related to the start time of transition that the paper tries to answer are, (i) which state variable better identifies it, (ii) does it exhibits any seasonal variation and (iii) does it shows any height dependency? (i) Among all state variables, the decrease of temperature at the surface and SNR aloft are strikingly apparent in all case studies, which makes them ideal to identify the start time of AET. Further, the distributions of $\text{Trans}_{\text{sunset}}$ for T and SNR are somewhat consistent and narrower than that for other state variables. Although several earlier studies employed reversal of sign in surface heat flux as a criterion for transition (Lothan et al., 2014 and references therein), it is now well known that such a reversal not always occurs during the transition (Busse and Knupp, 2012). The formation of an inversion depends on several other

ACPD
14, 31483–31514, 2014

factors and therefore the formation of inversion alone cannot be used to define the transition. A few studies used deceleration of low-level wind as a criterion for identifying the transition (Mahrt, 1981). The above criterion works well in the lower portion of ABL, but fails above the nocturnal boundary layer, where the wind accelerates in the frictionless fluid. Therefore, T at the surface and SNR aloft can be used to identify the start of time of transition unambiguously, as also suggested by Edwards et al. (2006). (ii) The start time of transition as defined by different state variables shows some seasonal variation, with late transitions during the northeast monsoon season. Though Gadanki receives 55 % of the annual rainfall in the southwest monsoon, rising instantaneous soil moisture levels, but the high insolation and temperatures immediately consume the soil moisture for latent heating. On the other hand, this region also gets good amount of rainfall during the cool northeast monsoon (Rao et al., 2009). The soil moisture levels, therefore, remain high in this season. It is known from earlier studies that the abundance of soil moisture not only produces shallow ABL but also delays the growth of the ABL (Sandeep et al., 2014). It appears from present observations that not only the growth but also the collapse (or transition) is getting delayed due to the excess soil moisture. (iii) The total and seasonal distributions of $\mathrm{Trans}_{\mathrm{sunset}}$ for different state variables at the surface and aloft clearly show the height dependency in the start time of transition, following a top-to-bottom evolution. It is known from the literature that there exists an apparent contradiction between those who think the transition starts in the afternoon at high levels (Angevine, 2008) and others who believe the AET occurs around the sunset and follows a bottom-up evolution. The present study supports the former view, as similar evolution is seen in total and seasonal plots (Figs. 3 and 4). During the AET, when the surface buoyancy flux decreases toward zero, the influence of other competing processes like advection, and entrainment becomes relatively more important (Bosveld et al., 2014). Therefore an attempt has been made to estimate these fluxes (buoyancy and entrainment) to understand their roles in the observed height dependency in transition start time.

ACPD
14, 31483–31514, 2014

The ratio between the vertical kinematic eddy heat flux at the top of ABL and kinematic eddy heat flux at the surface (entrainment ratio) (Sun et al., 2008), as given below, therefore, becomes a fundamental and decisive parameter.

$$A_r = -\frac{\overline{(w|\theta|)}_{z_i}}{\overline{(w|\theta|)}_s} \quad (1)$$

The heat flux at the top of ABL (or entrainment flux) is estimated following Angevine (1999). The entrainment can occur due to any or all of these factors, (1) when there is a shift in the ABL height (2) due to wind shear at the top of the ABL and (3) due to wind shear at the surface.

$$-\overline{(w|\theta|)}_{z_i} = A_0 + (A_2 u_*^2 \overline{u} + A_3 \Delta u_h^3) \cdot (\theta_{vo}/g d_1), \quad (2)$$

where u^* is the friction velocity, u the surface horizontal velocity (5 m in our case), Δu_h the wind shear at the top of ABL, g the acceleration due to gravity, θ_{vo} the virtual potential temperature at the surface, d_1 is the depth of entrainment zone and A_2 and A_3 are empirical constants, $A_2 = 0.005$ and $A_3 = 0.01$ (Stull, 1976). A_0 is the entrainment flux in the absence of any mechanical term contribution and is expressed as $w_e \Delta\theta$, w_e is the entrainment velocity and is estimated as follows

$$w_e = \frac{dz_i}{dt} - \overline{w} \quad (3)$$

where $\overline{w}$ is the average vertical velocity at the top of ABL and $\Delta\theta$ the vertical gradient in θ_v at the top of ABL.

It is clear from above equations that profiles of meteorological parameters such as T, RH/r and w are essential to estimate the entrainment ratio. Though w can be obtained continuously from the wind profiler, continuous measurement of T and RH/r at the top of ABL is a difficult task. We, therefore, considered two 3 days campaign data (one

ACPD
14, 31483–31514, 2014

each from southwest monsoon and winter), wherein radiosonde ascents were made once in ~ 3 h, for a detailed study.

Figure 5a–c shows the time-height variation of SNR, w and σ on 22 July 2011, depicting the typical diurnal evolution of ABL during the campaign period. The θ_v profiles during morning-evening (at 08:24, 11:54, 14:25 and 17:15 IST) period are shown in Fig. 5d to depict the height of ABL (and also the gradients in θ_v at the top of the ABL). Clearly, the height of ABL as obtained by the profiler (shown with dots on SNR plot) and radiosonde (the gradient in θ_v profile) corresponds well. The agreement between them is also good in the diurnal variation, with both the measurements showing shallow ABL in the morning and evening transition periods and deep ABL during the day, when the ABL is convectively active.

The start time of AET as seen by different state variables at the surface and aloft on all days during the two campaigns is shown in Fig. 6a and b. It clearly reiterates the height dependency of start time of AET seen in Figs. 2–4, i.e., the start time of AET observed by the profiler precedes surface state variables on all days and in both seasons. Though the same pattern is seen on all days, but the time at which the transition starts varies considerably from day to day.

The entrainment flux at the top of ABL is estimated by combining the measurements of radiosonde ($\Delta\theta$, d_1), profiler (w, Δu_h), MBLM (u, θ_{vo}) and a meteorological flux tower (u^*). The sensible heat flux and u^* at the surface required to quantify the entrainment ratio (Eq. 1) are estimated following the eddy covariance method by using 20 Hz resolution ultrasonic anemometer measurements at 8 m level. A stringent data quality check has been performed for the estimation of fluxes (Burba, 2013). These fluxes are evaluated at 30 min resolution.

Figure 6c and d shows the sensible and entrainment fluxes at ~ 3 h resolution during the day, depicting the forcing on ABL from bottom and top. The sensible heat flux varies considerably during the day, with fluxes varying from 1.5–2.5 K ms^{-1} around noon (~ 11:00 and ~ 14:00 IST) to 0.02–0.07 K ms^{-1} during the morning and evening transitions (~ 08:00 and ~ 17:00 IST). On the other hand, the entrainment flux neither

ACPD
14, 31483–31514, 2014

changes drastically during the day nor shows a clear diurnal cycle (compared to sensible heat flux). The magnitude of entrainment flux depends mostly on the first term in Eq. (2), while the shear (2 and 3 terms in Eq. 2) contributes very little to the total entrainment flux (not shown). In contrast to large eddy simulations (LES) by Canut et al. (2012), who found an increase of the entrainment rate in the late afternoon, the present observations do not show any such increase, rather the entrainment flux remained constant throughout the day on all days. Since the buoyancy flux changes considerably, the entrainment ratio varies significantly during the course of the day. The entrainment ratio increases to 0.5–1.1 during the morning and evening transitions. Therefore, it is very clear from these observations that the forcing from the top (i.e., entrainment flux) becomes very important and plays a decisive role in altering the structure of ABL. It is known from earlier studies by Lohou et al. (2010) that the entrainment not only modifies the top of the ABL but also impacts the entire depth of the ABL. Also, with continuous waning of sensible heat flux during the AET, both the vertical extent and strength of thermals (can be seen in Figs. 1 and 5) decrease monotonously. At the same time, the surface forcing (heating) remains good enough to maintain the turbulence close to the surface and therefore does not show the signature of transition, but delays it at the surface (Angevine, 2008). The reduction in the vertical extent and strength of thermals and an increase in entrainment ratio appear to be primarily responsible for the observed top-to-bottom evolution of the start time of AET.

5 Conclusions

This study presents a comprehensive view on the AET in terms of understanding the variability of different state variables using a suite of in situ and remote sensing measurements at Gadanki. The study aims to address the following issues related to the start time of AET with a unique and statistically robust dataset (~ 3 years). Which parameter first shows the signature of transition at the surface and aloft? Which parameter better defines or identifies it? Does it follows any seasonal cycle? How does it varies

ACPD
14, 31483–31514, 2014

with altitude? (i) Among the surface state variables, the signature of transition is first seen in σ^2_{ws} and T data, both of which start decreasing monotonically ∼ 100 min prior to the time of sunset. The r increase is the last signature of transition, while the reversal of sensible heat flux (in terms of ΔT variation from positive to negative) falls in between these extremes. Aloft, both SNR and σ identify the start of AET at the same time, 120–160 min prior to the time of sunset, depending on the height considered. The observed mean start time of AET (2 h prior to the sunset), obtained from SNR and σ variations, matches well with that obtained by Mahrt (1981), who used horizontal wind reduction for identifying the transition. (ii) At the surface, the start time of AET can be discerned more easily from variations of T than from that of σ^2_{ws}, r and ΔT. While σ^2_{ws} and ΔT variations show large modulations with time, r variation is ambiguous at times. Also, the temperature reduction is more consistent with relatively narrow distribution and occurs always before the sunset. Aloft, SNR variation is robust in identifying the transition compared to ambiguous variations in horizontal wind velocity (decreases at lower altitudes and increases at higher altitudes). (iii) The start time of AET as defined by different state variables show some seasonal variation, with delayed transitions during the northeast monsoon at the surface and aloft. Though there is some seasonal variation in the start time of AET relative to sunset time, the order in which the signature of AET is seen in different state variables (first in T, and σ^2_{ws} followed by ΔT and r) remained nearly the same in all seasons. (iv) Interestingly, the start time of AET exhibits a clear height dependency, i.e., the signature of transition is seen first in profiler attributes (∼ 160 min) followed by sodar attributes (∼ 120 min) and finally in surface state variables (100 min), suggesting that the transition follows a top-to-bottom evolution (Angvine, 2008). The fact that the first signatures of transition are seen at higher altitudes by profiler/sodars than at the surface suggests that the forces other than the buoyancy could also play an important role during the transition. With continuous waning of sensible heat flux (and surface forcing) during the AET, both the vertical extent and strength of thermals decrease steadily (as seen in Figs. 1 and 5), triggering the collapse of ABL or transition. However, the surface heating is good enough to maintain

ACPD
14, 31483–31514, 2014

the state variables and delay the decrease of T and σ^2_{ws} (considered to be the signatures of transition). Further, the impact of forcings from top and bottom on the ABL is studied by quantifying the sensible and entrainment fluxes, using a flux tower and profiler-radiosonde measurements, respectively. Though the sensible heat flux varied significantly during the day, the entrainment flux remained nearly the same throughout the day. The entrainment ratio increases considerably during the morning and evening transitional periods. The reduction in the strength and vertical extent of thermals and an increase in entrainment ratio are thought be responsible for the observed top-to-bottom evolution of the transition.

Acknowledgements. The authors would like to thanks M. Venkat Ratnam for providing the GPS radiosonde used in the present study (experiments are conducted under the special campaign of Tropical Tropopause Dynamics (TTD) as a part of CAWSES-Phase II programme, India).

References

Acevedo, O. C. and Fitzjarrald, D. R.: The early evening surface-layer transition: temporal and spatial variability, J. Atmos. Sci., 11, 2650–2667, 2001.

Anandan, V. K., Shravankumar, M., and Srinivasarao, I.: First results of experimental tests of newly developed NARL phased array Doppler sodar, J. Atmos. Ocean. Tech., 25, 1778–1784, 2008.

Angevine, W. M.: Entrainment results including advection and case studies from the Flatland boundary layer experiments, J. Geophys. Res., 104, 30947–30963, 1999.

Angevine, W. M.: Transitional, entraining, cloudy, and coastal boundary layers, Acta Geophys., 56, 2–20, 2008.

Beare, R. J., Edwards, J. M., and Lapworth, A. J.: Simulation of the observed evening transition and nocturnal boundary layers: large–eddy modelling, Q. J. Roy. Meteor. Soc., 132, 61–80, 2006.

Bonin, T., Phillip, C., Brett, Z., and Fedorovich, E.: Observations of the early evening boundary-layer transition using a small unmanned aerial system, Bound.-Lay. Meteorol., 146, 119–132, 2013.

ACPD
14, 31483–31514, 2014

Bosveld, F. C., Baas, P., Steeneveld, G. J., Holtslag, A. A. M., Angevine, W. M., Bazile, E., Bruijn, E. I. F. D., Deacu, D., Edwards, J. M., Michael, E. K., Larson, V. E., Pleim, J. E., Raschendorfer, M., and Svensson, G.: The third GABLS intercomparison case for evaluation studies of boundary-layer models. Part B: Results and process understanding, Boundary-Lay. Meteorol., 152, 157–187, doi:10.1007/s10546-014-9919-1, 2014.

Brazel, A. J., Fernando, H. J. S., Hunt, J. C. R., Selvor, N., Hedquist, B. C., and Pardyjak, E.: Evening transition observations in Phoenix, Arizona, J. Appl. Meteorol., 44, 99–112, 2005.

Burba, G.: Eddy Covariance Method for Scientific, Industrial, Agricultural, and Regulatory Applications, LI-COR Biosciences, Nebraska, 331 pp., 2013.

Busse, J. and Knupp, K.: Observed characteristics of the afternoon-evening boundary layer transition based on sodar and surface data, J. Appl. Meteorol., 51, 571–582, 2012.

Canut, G., Couvreux, F., Lothon, M., Pino, D., and Said, F.: Observations and large-eddy simulations of entrainment in the sheared Sahelian bounday layer, Bound.-Lay. Meteorol., 142, 79–101, doi:10.1007/s10546-011-9661-x, 2012.

Edwards, J. M., Beare, R. J., and Lapworth, A. J.: Simulation of the observed evening transition and nocturnal boundary layers: single-column modelling, Q. J. Roy. Meteor. Soc., 132, 61–80, 2006.

Fernando, H. J. S., Verhoef, B., Sabatino, S. D., Leo, L. S., and Park, S.: The Phoenix evening transition flow experiment (TRANSFLEX), Bound.-Lay. Meteorol., 147, 443–468, doi:10.1007/s10546-012-9795-5, 2013.

Grant, A. L. M.: An observational study of the evening transition boundary-layer, Q. J. Roy. Meteor. Soc., 123, 657–677, 1997.

Grimsdell, A. W. and Angevine, W. M.: Observations of the afternoon transition of the convective boundary layer, J. Appl. Meteorol., 41, 3–11, 2002.

Klein, P. M., Hu, X. M., and Xue, M.: Impacts of mixing processes in nocturnal atmospheric boundary layer on urban ozone concentrations, Bound.-Lay. Meteorol., 150, 107–130, doi:10.1007/s10546-013-9864-4, 2014.

Lohou, F., Said, F., Lothon, M., Durand, P., and Serça, D.: Impact of boundary layer processes on near-surface turbulence within the West Africa monsoon, Bound.-Lay. Meteorol., 136, 1–23, 2010.

Lothon, M., Lohou, F., Pino, D., Couvreux, F., Pardyjak, E. R., Reuder, J., Vilà-Guerau de Arellano, J., Durand, P, Hartogensis, O., Legain, D., Augustin, P., Gioli, B., Lenschow, D. H., Faloona, I., Yagüe, C., Alexander, D. C., Angevine, W. M., Bargain, E, Barrié, J., Bazile, E.,

ACPD
14, 31483–31514, 2014

Bezombes, Y., Blay-Carreras, E., van de Boer, A., Boichard, J. L., Bourdon, A., Butet, A., Campistron, B., de Coster, O., Cuxart, J., Dabas, A., Darbieu, C., Deboudt, K., Delbarre, H., Derrien, S., Flament, P., Fourmentin, M., Garai, A., Gibert, F., Graf, A., Groebner, J., Guichard, F., Jiménez, M. A., Jonassen, M., van den Kroonenberg, A., Magliulo, V., Martin, S., Martinez, D., Mastrorillo, L., Moene, A. F., Molinos, F., Moulin, E., Pietersen, H. P., Piguet, B., Pique, E., Román-Cascón, C., Rufin-Soler, C., Saïd, F., Sastre-Marugán, M., Seity, Y., Steeneveld, G. J., Toscano, P., Traullé, O., Tzanos, D., Wacker, S., Wildmann, N., and Zaldei, A.: The BLLAST field experiment: Boundary-Layer Late Afternoon and Sunset Turbulence, Atmos. Chem. Phys., 14, 10931–10960, doi:10.5194/acp-14-10931-2014, 2014.

Mahrt, L.: The early evening boundary layer transition, Q. J. Roy. Meteor. Soc., 107, 329–343, 1981.

Nadaeau, D. F., Pardyjak, E. R., and Higgins, C. W.: A simple model for the afternoon and early decay of convective turbulence over different land surfaces, Bound.-Lay. Meteorol., 141, 301–324, 2011.

Nieuwstadt, F. T. M. and Brost, R. A.: The decay of convective turbulence, J. Atmos. Sci., 43, 532–546, 1986.

Pino, D., Jonker, H. J. J., Arellano, J. V. G., and Dosio, A.: Role of shear and the inversion strength during sunset turbulence over land: characteristic length scales, Bound.-Lay. Meteorol., 121, 537–556, doi:10.1007/s10546-006-9080-6, 2006.

Poulos, S. G., Blumen, W., Fritts, D. C., Lundquist, J. K., Sun, J., Burns, S. P., Nappo, C., Banta, R., Newsom, R., Cuxart, J., Terradellas, E., Balsley, B., and Jensen, M.: A comprehensive investigation of the stable nocturnal boundary layer, B. Am. Meteorol. Soc., 83, 555–581, 2002.

Rao, T. N., Rao, D. N., and Mohan, K.: Classification of tropical precipitating systems and associated Z–R relationships, J. Geophys. Res., 116, 17699–17711, 2001.

Rao, T. N., Kirankumar, N. V. P., Radhakrishna, B., Rao, D. N., and Nakamura, K.: Classification of tropical precipitating systems using wind profiler spectral moments part I: algorithm description and validation, J. Atmos. Ocean. Tech., 25, 884–897, doi:10.1175/2007JTECHA1031.1, 2008.

Rao, T. N., Radhakrishna, B., Nakamura, K., and Prabhakara Rao, N.: Differences in raindrop size distribution from southwest monsoon to northeast monsoon at Gadanki, Q. J. Roy. Meteor. Soc., 135, 1630–1637, 2009.

ACPD
14, 31483–31514, 2014

Reddy, K. K., Kozu, T., Nakamura, K., Ohno, Y., Srinivasulu, P., Anandan, V. K., Jain, A. R., Rao, P. B., Rao, R. R., Vishwanathan, G., and Rao, D. N.: Lower atmospheric wind profiler at Gadanki, tropical India: Initial results, Meteorol. Z., 10, 457–466, 2001.

Sandeep, A., Rao, T. N., Ramkiran, C. N., and Rao, S. V. B.: Differences in atmospheric boundary-layer characteristics between wet and dry episodes of the Indian summer monsoon, Bound.-Lay. Meteorol., 153, 217–236, doi:10.1007/s10546-014-9945-z, 2014.

Sastre, M., Yagüe, C., Román-Cascón, C., Maqueda, G., Salamanca, F., and Viana, S.: Evening transitions of the atmospheric boundary layer: characterization, case studies and WRF simulations, Adv. Sci. Res., 8, 39–44, doi:10.5194/asr-8-39-2012, 2012.

Sorbjan, Z.: A numerical study of daily transitions in the convective boundary layer, Bound.-Lay. Meteorol., 123, 365–383, doi:10.1007/s10546-006-9147-4, 2007.

Srinivasulu, P., Yasodha, P., Kamaraj, P., Jayaraman, A., Reddy, S. N., and Satyanarayana, S.: Simplified active array L-band radar for atmospheric wind profiling: initial results, J. Atmos. Ocean. Tech., 28, 1436–1447, doi:10.1175/JTECH-D-11-00011.1, 2011.

Srinivasulu, P., Yasodha, P., Kamaraj, P., Rao, T. N., Jayaraman, A., Reddy, S. N., and Satyanarayana, S.: 1280-MHz active array radar wind profiler for lower atmosphere: system description and data validation, J. Atmos. Ocean. Tech., 29, 1455–1470, doi:10.1175/JTECH-D-12-00030.1, 2012.

Stull, R. B.: The energetics of entrainment across a density interface, J. Atmos. Sci., 33, 1260–1267, 1976.

Sun, J. and Wang, Y.: Effect of the entrainment flux ratio on the relationship between entrainment rate and convective Richardson Number, Bound.-Lay. Meteorol., 126, 237–247, doi:10.1007/s10546-007-9231-4, 2008.

Van de Wiel, B. J. H., Moene, A. F., Steenveld, G. J., Baas, P., Bosveld, F. C., and Holtslag, A. A. M.: A conceptual view on inertial oscillations and nocturnal low-level jets, J. Atmos. Sci., 67, 2679–2689, doi:10.1175/2010JAS3289.1, 2010.

ACPD
14, 31483–31514, 2014

Table 1. Instruments used in the integrated approach, their operating frequency, height coverage, vertical and temporal resolutions and duration of data.

Instrument	Frequency of operation	Measured parameters	Height coverage	Vertical resolution	Temporal resolution	Period used
SODAR	1.8 kHz	SNR, winds and σ	0.03–1.5 km	30 m	30 s	2007–2010
LAWP	1.357 GHz	SNR, winds and σ	0.3–4.2 km	150 m	~ 11 min	1999–2000
$WPR_{8\times8}$	1.280 GHz	SNR, winds and σ	0.3–6.15 km	150 m	~ 10 min	2010
$WPR_{16\times16}$	1.280 GHz	SNR, winds and σ	0.75–5.025 km	75 m	~ 10 min	2010–2011
MBLM		T, RH, pressure, WS, WD and solar radiation	5–15 m	5 m	1 s	2009–2011
GPS Radiosonde		Temperature, pressure and relative humidity	0–30 km	100 m	3 h	17–19 Jan 2011 21–24 Jul 2011
50 m Tower		Sonic temperature, vertical wind	8 m		0.05 s	17–19 Jan 2011 21–24 Jul 2011

ACPD
14, 31483–31514, 2014

Table 2. Details of sensors (make, model number, resolution and accuracy) on MBLM.

Sensor	Make	Model No.	Resolution	Measurement height	Accuracy
Wind Speed and Wind Direction	RM Young	05103V	1 Hz	5, 10 and 15 m	0.3 m s^{-1}, 2°
Temperature and Relative humidity	Rotronics	Hygroclip S3	1 Hz	5, 10 and 15 m	0.1 °C, 2 %
Pressure	Komoline	KDS-021	1 Hz	1.2 m	1 hPa
Short Wave Radiation	Kipp and Zonen	CMP 6	1 Hz	1.2 m	1 W m^{-2}

ACPD
14, 31483–31514, 2014

Table 3. Major specifications of SODAR, LAWP, $WPR_{8\times8}$ and $WPR_{16\times16}$.

Parameter	SODAR	LAWP	$WPR_{16\times16}$	$WPR_{8\times8}$
Operating frequency	1.8 kHz	1357.5 MHz	1280 MHz	1280 MHz
Peak power	100 W	1 kW	1.2 kW	0.8 kW
Antenna array	1 m × 1 m	2 m × 2 m	2.8 m × 2.8 m	1.4 m × 1.4 m
Pulse width	180 ms	1 µs (uncoded)	4 µs (coded)	1 µs (uncoded)
Inter pulse period (µs)	9×10^6	40	55	55
No. of Coherent Integrations	1	70	64	32
No. of Incoherent Integrations	1	100	20	20
No. of FFT points	4096	128	1024	1024
Beam width (deg)	4	3	5	6.5
Range resolution (m)	30	150	75	150
Beam directions*	N16, Z, E16	E15, Z, N15	E15, W15, Z, N15, S15	E10N10, W10S10, Z, W10N10, E10S10

* E, W, Z, N and S denote east, west, zenith, north and south directions, respectively, and the number indicates the off-zenith angle.

ACPD
14, 31483–31514, 2014

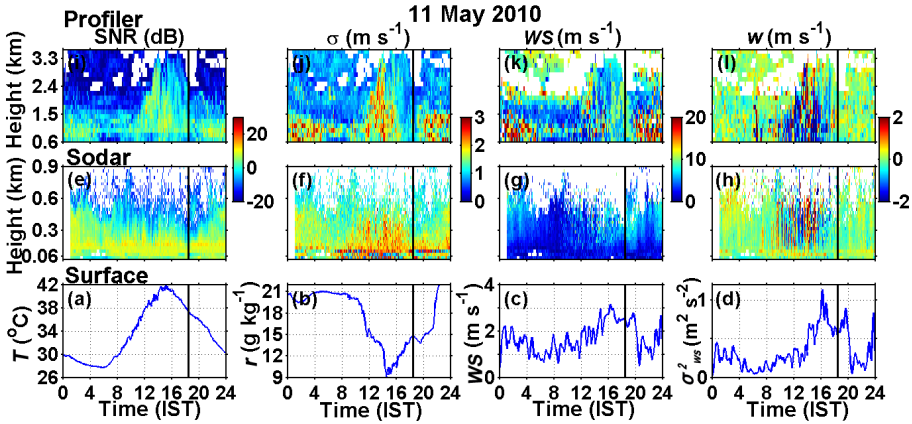

Figure 1. Diurnal variation of state variables at the surface and aloft on 11 May 2010, MBLM-derived surface **(a)** T, **(b)** r, **(c)** WS and **(d)** σ^2_{WS} and sodar-derived **(e)** SNR, **(f)** σ, **(g)** WS and **(h)** w. **(i–l)** same as **(e–h)**, except for profiler-derived state variables. The solid vertical line indicates the time of sunset.

ACPD
14, 31483–31514, 2014

A comprehensive investigation of the atmospheric boundary layer

A. Sandeep et al.

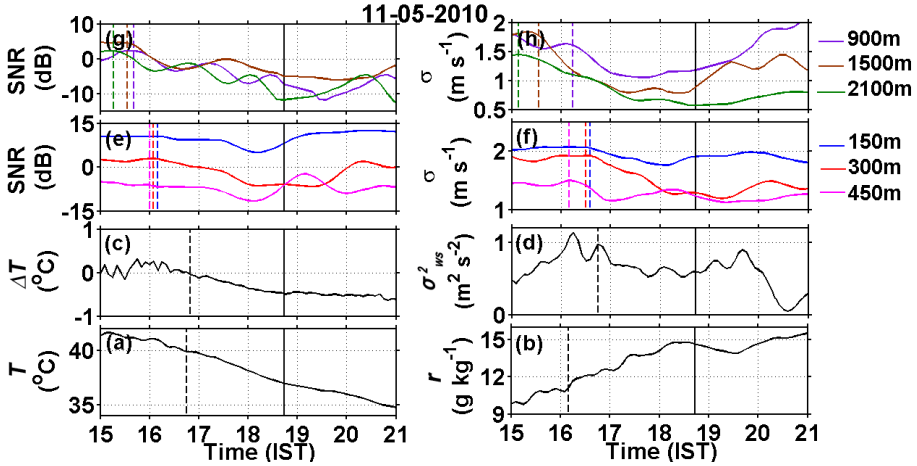

Figure 2. Temporal variation of state variables (at the surface and aloft) few hours before and after the time of sunset (indicated with a black solid vertical line). Temporal variation of MBLM-derived **(a)** T, **(b)** r, **(c)** ΔT and **(d)** σ^2_{WS}, sodar-derived **(e)** SNR and **(f)** σ and profiler-derived **(g)** SNR and **(h)** σ. The sodar- and profiler-derived parameters are plotted at 3 representative levels each (150, 300 and 450 m for sodar and 900, 1500 and 2100 m for profiler). Vertical dashed lines indicate the start time of the transition as identified by different state variables.

ACPD
14, 31483–31514, 2014

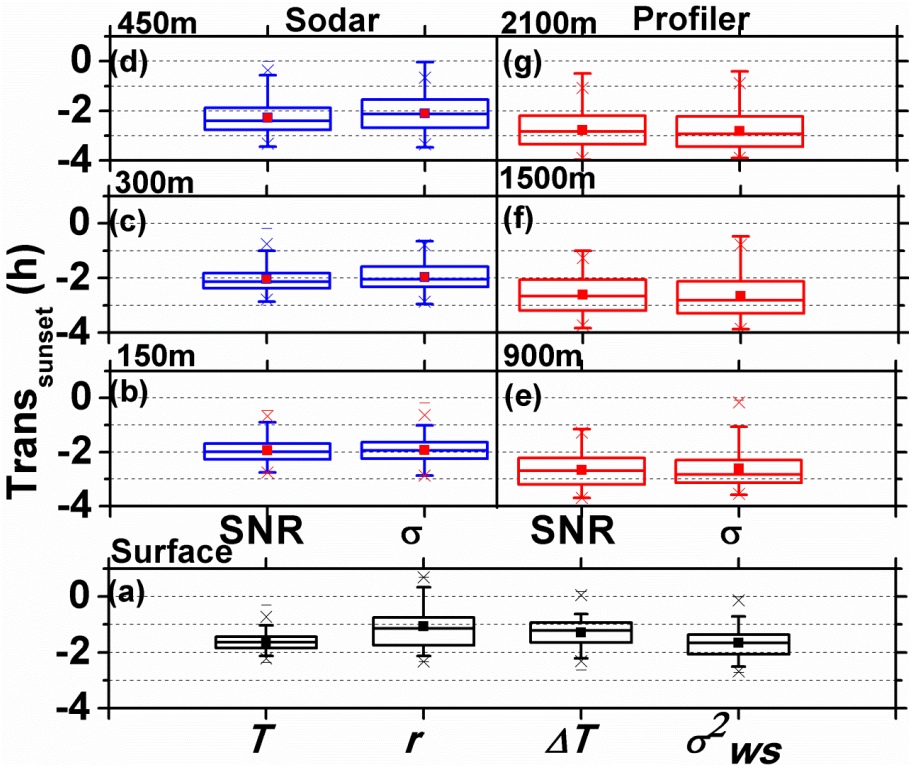

Figure 3. Distributions (in terms of box plot) of $Trans_{sunset}$ (=start time of AET – time of sunset) for different state variables, depicting the behaviour of transition start time with reference to the sunset time. Distributions for $Trans_{sunset}$ at **(a)** the surface (obtained from T, r, ΔT and σ^2_{WS}), **(b–d)** 150, 300 and 450 m, respectively (obtained from sodar-derived SNR and σ) and **(e–g)** 900, 1500 and 2100 m, respectively (obtained from profiler-derived SNR and σ).

ACPD
14, 31483–31514, 2014

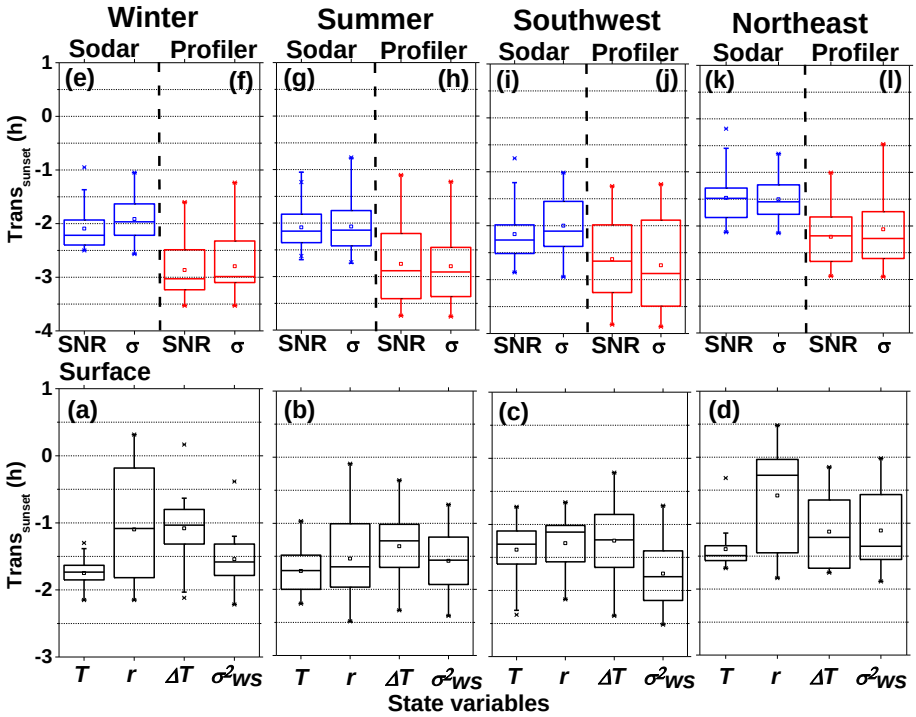

Figure 4. The distributions of $Trans_{sunset}$ as obtained by different surface state variables for **(a)** winter **(b)** premonsoon, **(c)** southwest monsoon and **(d)** northeast monsoon, depicting the seasonal variability in the start time of transition. The distributions for $Trans_{sunset}$ as obtained by sodar-derived SNR and σ at 300 m for **(e)** winter, **(g)** premonsoon, **(i)** southwest monsoon and **(k)** northeast monsoon, respectively. (**f**, **h**, **j** and **l**) are same as (**e**, **g**, **i** and **k**), except for profiler-derived SNR and σ at 1500 m.

ACPD
14, 31483–31514, 2014

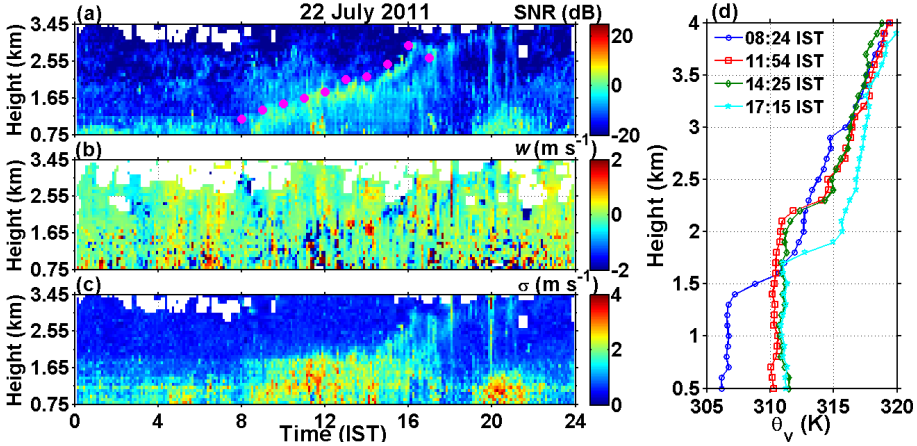

Figure 5. Diurnal variation of RADAR attributes **(a)** SNR **(b)** w and **(c)** σ on 22 July 2011, illustrating the evolution of ABL and evening transition. **(d)** The vertical variation of radiosonde-derived θ_v at ~ 3 h intervals. The solid symbols on **(a)** indicate the height of ABL.

ACPD
14, 31483–31514, 2014

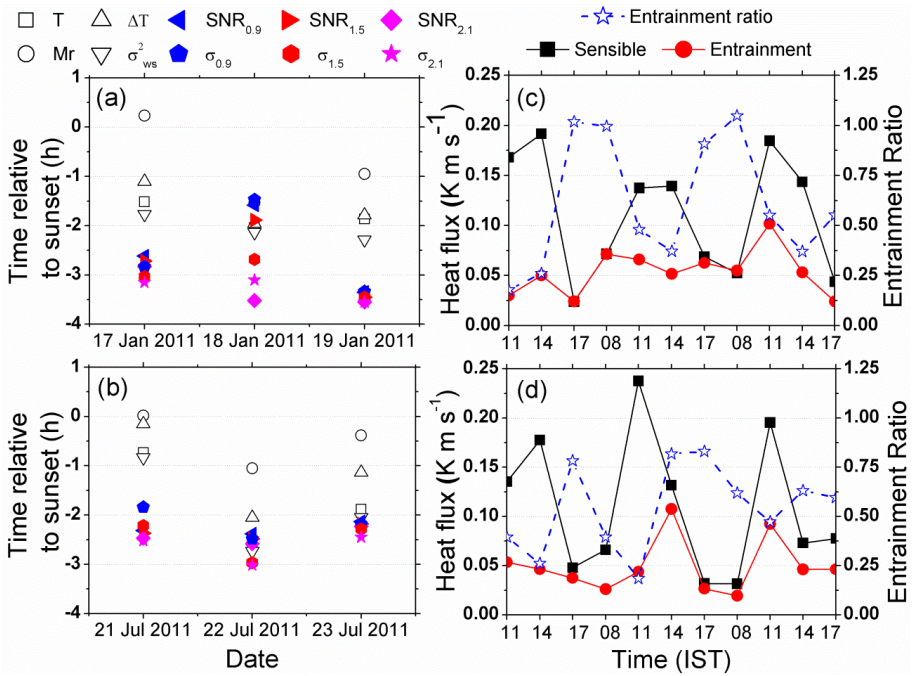

Figure 6. The start time of AET with reference to the time of sunset as obtained by different state variables at the surface and aloft during **(a)** 17–19 January 2011 and **(b)** 21–23 July 2011. **(c)** and **(d)** Sensible and entrainment fluxes (left axis) and entrainment ratio (right axis) estimated at ~ 3 h intervals for the above days, indicating the forcing's on ABL from the bottom and top.

ACPD
14, 31483–31514, 2014